Journal of Power Sources 263 (2014) 98–103

Contents lists available at ScienceDirect

Journal of Power Sources

journal homepage: www.elsevier.com/locate/jpowsour

Understanding dynamics of polysulfide dissolution and re-deposition in working lithium–sulfur battery by in-operando transmission X-ray microscopy

Chia-Nan Lin [a], Wen-Chin Chen [a], Yen-Fang Song [b,*], Chun-Chieh Wang [b], Li-Duan Tsai [c], Nae-Lih Wu [a,*]

[a] Department of Chemical Engineering, National Taiwan University, Taipei 10617, Taiwan, ROC
[b] National Synchrotron Radiation Research Center, Hsinchu 30077, Taiwan, ROC
[c] Industrial Technology Research Institute, Hsinchu 31040, Taiwan, ROC

HIGHLIGHTS

- Polysulfide (PS) dissolution and re-deposition in working Li–S electrode is studied.
- Particle size variation of S electrode is monitored by transmission X-ray microscopy.
- Extensive shrinking and expansion of S particles are observed.
- Solubility of PS is strongly dependent on Li content.
- PS re-deposition is nucleation-limited and leads to sulfur aggregation.

GRAPHICAL ABSTRACT

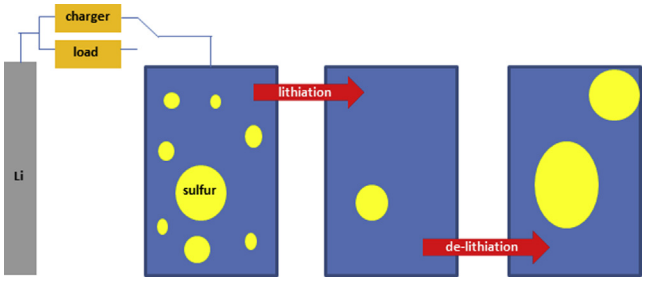

ARTICLE INFO

Article history:
Received 24 January 2014
Received in revised form
14 March 2014
Accepted 2 April 2014
Available online 12 April 2014

Keywords:
Lithium–sulfur batteries
Transmission X-ray microscopy
Dissolution
Re-deposition
Nucleation

ABSTRACT

The dynamics of polysulfide (PS) dissolution and re-deposition during electrochemical charge/discharge of the lithium-sulfur (Li–S) cell has been investigated in a quantitative manner based on in-operando transmission X-ray microscopy (TXM) analysis of dimensional variations of S particles in working cells that have been subjected to different depths of charge/discharge. Extensive shrinkage and expansion of S particles have been observed to result from PS dissolution and re-deposition, respectively. The dissolution rate of PS is found to have complex dependence on the Li content, being significantly higher for the stoichiometries of LiS_8 and Li_2S_4 than those between Li_2S_8 and Li_2S_6. PS re-deposition is nucleation-limited, leading to considerable aggregation of the S-containing active mass and enormous dimensional variations of active particles. These two consequences may impose threat to the cycle stability of the electrode. Possible benefit of introducing favorable nucleation sites is discussed.

1. Introduction

The development of high-energy-density rechargeable batteries becomes increasing important for clean and efficient energy storage and conversion technologies. Lithium–sulfur (Li–S) battery is a promising rechargeable battery system that has both high theoretical capacity (1675 mAh g^{-1}) and energy density (2600 Wh kg^{-1}) [1–8]. Moreover, S is inexpensive and nontoxic, making Li–S cell potentially suitable for large-scale energy storage applications. S lithiation during the operation of Li–S battery is a multi-step electrochemical process that involves different lithium

* Corresponding authors.
E-mail addresses: song@nsrrc.org.tw (Y.-F. Song), nlw001@ntu.edu.tw, naelihwu@yahoo.com (N.-L. Wu).

http://dx.doi.org/10.1016/j.jpowsour.2014.04.003
0378-7753/

polysulfide (PS) intermediates, some of which are highly soluble in the aprotic organic electrolyte. PS dissolution is a critical issue for the Li–S battery, as it has directly been linked to the deterioration of several key performance indexes, such as cycle life, self-discharge and coulombic efficiency, of the battery [9–15].

A few in-operando analytical techniques have been employed to probe different aspects of the PS dissolution process. Cañas et al. [16] conducted in-operando X-ray diffraction study on the evolution of the S-containing crystalline components during electrochemical charge/discharge cycles. Patel et al. [17] applied in-operando ultraviolet/visible (UV–Vis) spectroscopy to identify the development of dissolved PS species in the electrolyte. The results from both studies indicated extensive PS dissolution during charge/discharge cycles of Li–S cells. We have previously demonstrated that transmission X-ray microscopy (TXM) [18,19] allows for the possibility of in-operando study on microstructural evolution of active materials in working Li-ion battery electrodes. Nelson et al. [20] once reported an in-operando TXM study on the morphological changes of individual S particles during a deep charge/discharge cycle of a Li–S cell. Their results, surprisingly showing very little change in S particle size, are quite different from what would be expected from PS dissolution, and therefore may need further verification. Furthermore, while attention has been drawn mostly around the dissolution issue, re-deposition of S/PS taking place during de-lithiation and its potential impact on the performance of the Li–S battery have so far not been addressed.

Dimensional variation of electrode active material during charge/discharge is by itself of major interest for the development of viable battery. Large cyclic dimensional variation of active-material particles during the electrochemical processes, as well known to several Li-alloying anodes [21], is detrimental to the cycle stability of an electrode. The dissolution and re-deposition of PS may potentially lead to volumetric variations of individual S particles. Such dimensional variations have not been revealed.

In this study, the dynamics of PS dissolution and re-deposition has been investigated by analyzing, with in-operando TXM, the morphological variations of individual S particles in working Li–S cells that were subjected to different depths of charge/discharge. In contrast to what observed in the previous TXM report [20], the S active particles in the present work exhibit complex dimensional variations, both expansion and shrinkage, of which the kinetics shows strong dependence on the Li content and charge–discharge protocol. The kinetic aspects of PS dissolution/re-deposition have been treated in a quantitative manner based on the dimensional variations of the S particles. The implications of the observed dimensional variations of S particles on the performance of S electrode are discussed.

2. Experimental

2.1. Samples and electrode preparations

S powder was used as received (99.98%, Aldrich), and milled with a planetary high-energy ball-milling machine. The milling process was carried out for 10 h in air with a rotation speed of 300 rpm and a ball-to-powder weight ratio of 10:1. Electrochemical measurements were carried out by using the 2032-type coin-cells. The working electrode consisted of S particles, conductive additives and binder with weight ratios of 4:5:1, a composition similar to previous studies [16,20]. The conductive additives include graphitic flakes (99.9%; KS6, Timcal) and nano-size carbon black (99.9%; Super P, Timcal) with a weight ratio of 2:3. The binder was polyvinylidene fluoride (PVDF, Kynar). The working electrode was made by coating the slurry mixture onto an Al current collector. The electrode was then roll-compressed to a final thickness of ca. 45 μm, and the working electrode disks of 13 mm in diameter were punched off from the electrode. The counter electrode was a Li disk (15-mm diameter, 0.3-mm thick), and the electrolyte was 1 M solution of lithium bis(trifluoromethanesulfonyl)imide (LiTFSI; 99.95%, Aldrich) in 1,3-dioxolane (99.8%, Aldrich) and 1,2-dimethoxyethane (99.5%, Aldrich) (volume ratio 1:1). The covers on both sides of the cell were perforated and sealed with Kapton tapes in order to allow the X-ray beam to pass through the cell.

2.2. Electrochemical analysis

The charge/discharge tests were carried out on MCN6410 Arbin Battery Testing System with a constant current of 168 mA g^{-1} within the voltage window between 1.5 and 3.0 V.

2.3. Synchrotron TXM analyses

TXM study utilized the beam-line #01B1 facility of the National Synchrotron Radiation Research Center (NSRRC) in Taiwan, R.O.C. The light source operates with photon energy ranging between 8 and 11 keV. The X-rays passing through the tested coin cell goes through a zone plate optical system and then a phase ring to from the image. The field of view of a single image is 15 × 15 μm for the first order diffraction mode of zone plate. The phase ring positioned at the back focal plane of the zone plate results in a recording of the phase contrast images at the detector. A mosaic micrograph covering a larger area can be constructed from neighboring single-view images collected by shifting the sample stepwise with a motor. The electrochemical test was simultaneously carried out with a potentiostat connected to the tested coin cell.

3. Results and discussion

3.1. PS dissolution

Control studies were first carried out to ensure that X-ray illumination and aging alone (without simultaneous electrochemical action) has negligible effect on the dimension of the S particles. As shown in Fig. S1, illumination under the selected X-ray intensity for a period of 5 h did not cause appreciable change in the morphology of the S particles. Throughout this study, each TXM analysis was carried out for no longer than 5 h.

To study the dynamics of the dissolution process, a Li–S cell was subjected to a deep lithiation cycle, and the variation in particle morphology was monitored. Fig. 1a shows the mosaic TXM micrograph covering an actual area of 105 μm × 105 μm of a S electrode before the electrochemical treatment. The S particles, having a size distribution ranging from 3 μm to 12 μm and appearing as dark particles in the micrograph (phase-contrast mode), are embedded within a carbon matrix.

Fig. 2a shows a series of snapshots that focus on an area that contains three neighboring particles, respectively indexed as A (largest), B (medium) and C (smallest), at different moments ($t = 0$, 180, 230 min) during lithiation. The voltage-versus-time plot is shown in Fig. 2b (solid line). These particles and background (carbon) are color-coded in order to enhance the contrast (The same set of snapshots without color-coding is shown in Fig. S2 for comparison). As shown, all these particles exhibited extensive size reduction with increasing lithiation. At the end of the lithiation cycle, essentially all the original S particles in the examined area disappeared with the formation of new faceted large particles elsewhere (arrows in Fig. 1b), which are believed to be insoluble

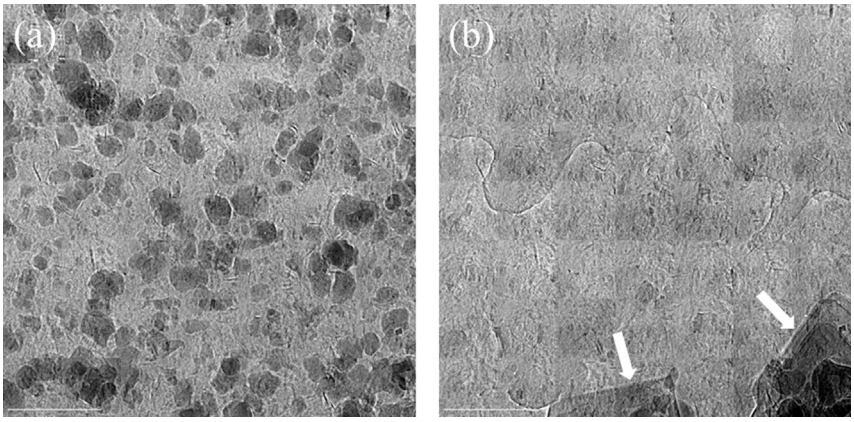

Fig. 1. Mosaic TXM micrographs of a sulfur electrode (a) before and (b) after deep electrochemical lithiation. The arrows points to the formation of large insoluble polysulfide particles.

polysulfide crystals, including Li_2S_2 and/or Li_2S. Clearly, tremendous migration and aggregation of the active material took place as a consequence of only one lithiation cycle. The cell was subsequently dissembled and analyzed by scanning electron microscopy. A large amount of S was found to deposit on one-side of the separator. This is consistent with the observation of Cañas et al. [16].

Fig. 2b gives detailed dimensional variations, expressed in terms of D/D_0, where D_0 is the initial particle dimension and D instantaneous dimension, as a function of lithiation time (lower x-axis, Fig. 2b) and Li content (upper x-axis) (Particle dimension is taken as the horizontal dimension passing through the center of a particle). For all of these particles, the shrinking behavior can be divided into three regions showing different shrinking rates, including faster rates during the initial and final stages (regions I and III, respectively) and a slower rate in between (region II). Region I occurs during the first ca. 50 min period, and it spans over slightly more than one-half of the first voltage plateau. Region II covers the rest portion of the first plateau and nearly the entire sloped portion between the two plateaus. Region III covers the initial period of the second plateau. It is important to note that all the particles completely dissolved when the electrode was discharged to the early stage of the second voltage plateau.

It is worth mentioning that, the total discharge capacity of the present S electrode, which contains "unprotected" large S particles, is only half of the theoretical capacity (for Li_xS, $x \sim 1.0$; solid line, Fig. 2b). For comparison, the voltage plot of another S electrode in which S is embedded within the pores of porous active carbon and which exhibits a capacity of 1200 mAh g^{-1} (Li_xS, $x \sim 1.5$; dashed line, Fig. 2b) is also shown. One notices that these two plots show essentially the same profile up to the beginning of the second plateau, and the difference resides mainly in the second-plateau capacity. That is, the capacity loss occurs over the period when the particles are seen to completely dissolve. The results indicate that PS dissolution followed by massive migration of the dissolved PS species out of the electrode constitutes a major cause to severe capacity loss.

In order to relate the dimensional variation to PS dissolution, we first consider the classical dissolution process from a smooth surface of a spherical particle having a diameter of D, the rate of volume reduction is equal to the mass flux multiplied by surface area and divided by density:

$$\frac{\pi D^2 f}{\rho} = -\frac{\mathrm{d}\left(\frac{1}{6}\pi D^3\right)}{\mathrm{d}t} \tag{1}$$

where ρ is the density of the dissolving particle and f, effective mass dissolution flux (mass/area-time). By integrating both sides, we obtain

$$\int_{D_0}^{D} \mathrm{d}D = -\int_{0}^{t} \frac{2f}{\rho}\mathrm{d}t \tag{2}$$

and

$$1 - \frac{D}{D_0} = \left(\frac{2f}{\rho D_0}\right)\cdot t = k\cdot t \tag{3}$$

where the proportionality constant, k, may be regarded as the normalized shrinking rate (min^{-1}) and expected to increase with decreasing initial particle size, D_0. Fig. 2c re-plots the particle size data according to Equation (3) based on the initial particle dimension prior to lithiation.

For region 1, the Li content expressed in Li_xS changes from $x = 0$ to 0.12, and it may be regarded as the transformation from S_8 to LiS_8: $S_8 + Li^+ + e^- \leftrightarrow LiS_8$. As shown, the dissolution behavior in this region is consistent with the derived dissolution equation; all the particles exhibits linear $[1 - D/D_0]$-vs.-t correlation, and the shrinking rate constant k, equal to the slope, increases with decreasing initial particle size. That is, the smaller particles shrink faster.

It should be mentioned that, other than PS dissolution, density change caused by Li insertion may also cause dimensional variation of S particles. The densities of PSs are not available, but it is known that there involves nearly 80% [2,10] increase in molar volume from S_8 to Li_2S. Intrapolation based on the molar volumes of these two end-members gives, for region I, an estimated volume expansion of 4.8% or a one-dimensional variation of 1.7%, which is negligible as compared with those shown in Fig. 2b.

Region II spans over the range of Li_xS from $x \sim 0.12$ to 0.36, which corresponds to the transformation from LiS_8 to nearly Li_2S_6: $LiS_8 + Li^+ + e^- \leftrightarrow Li_2S_8$; $3Li_2S_8 + 2Li^+ + 2e^- \leftrightarrow 4Li_2S_6$. The remarkably reduction in shrinking rate in this region as compared with region I is rather unexpected, as the general consensus is that the solubilities of long-chain (high S content) PSs might montonically increase with increasing Li content. The estimated volume change resulting from Li insertion, as described above, for this region is 9.6%, which corresponds to a one-dimensional enlargement of 3.0%. This possible enlargement is much smaller than the shrinkages observed in region I, and hence cannot be the main cause to the reduced shrinkage in region II. Therefore, the reduced

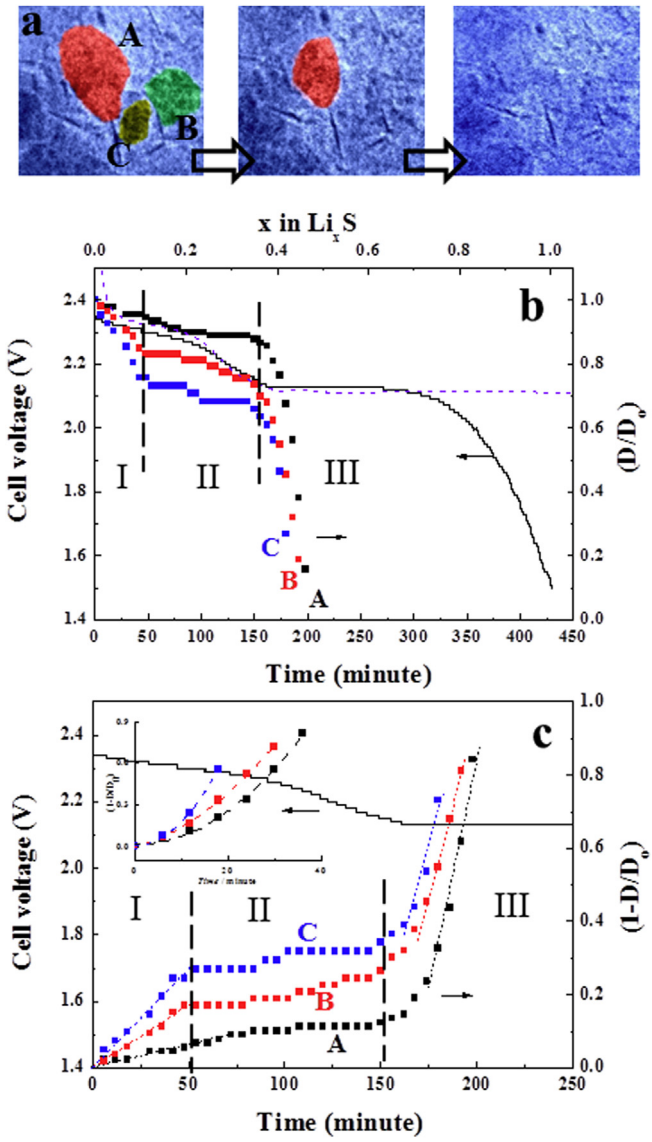

Fig. 2. TXM analysis of a S electrode subjected to a deep electrochemical lithiation; (a) snapshots of three particles, A, B, and C, taken at t = 0, 180, and 230 min, during lithiation; (b) plots of cell voltage (solid line) and dimensionless particle size (D/D_0) versus lithiation time (lower x-axis) and Li content (upper x-axis); a voltage plot of a second S electrode having higher lithiation capacity (dashed line) is also shown for comparison; (c) re-plots of particle size data in terms of extent of shrinkage, $1 - D/D_0$, according to Equation (3).

shrinkage rate in region II genuinely results from reduction in the dissolution rate of the PS species.

Finally, region III takes place during the early stage of the second plateau. All the particles exhibit accelerated shrinkage and completely disappear before the Li content x in Li_xS reaches 0.5, which corresponds to Li_2S_4. To correlate the dimension data with the shrinking model, we need to re-calculate the $[1 - D/D_0]$ data based on the particle sizes at the beginning of region III, and they are shown in the inset of Fig. 2c. The new plots show parabolic, rather than linear, correlation between $[1 - D/D_0]$ and time for all three particles. The concaveness of the plots indicates increasing instantaneous dissolution flux with time. The slope at any selected $[1 - D/D_0]$ value is found to increase with decreasing D_0; this is fundamentally consistent with Equation (3). Overall, the accelerating shrinking rate in region III may be attributed to a remarkable increase in solubility for Li_2S_4, and the shrinking rate accelerates as a result of increasing amount of Li_2S_4.

3.2. PS re-deposition

Because of massive migration of PS upon dissolution, it was not possible to monitor the re-deposition process of the same particle after it was completely dissolved. Therefore, the dynamics of re-deposition of PS was studied on a Li–S cell subjected to a series of shallow lithiation/de-lithiation cycles under region I condition (Fig. 3a). Fig. 3b shows the snapshots focusing on an area that also contains three neighboring particles (panel #i), including particles E (largest), F (medium) and G (smallest), at the selected moments indicated in Fig. 3a. Both particles E and F shrank during the first lithiation period (① in Fig. 3a), and particle F completely disappeared prior to the end of the lithiation (panel #ii). In contrast, the size of particle G did not changed.

During the initial stage of de-lithiation (② in Fig. 3a), the large particle E grew to exceed its original size (panel #iii). With further de-lithiation, more deposition took place in the areas surrounding particle E. Notably, deposit grew on particle G (panels #iv and #v). Upon the second lithiation (③ in Fig. 3a), both the newly deposited and pre-existing particles (such as particle E) showed size reduction (panel #vi). The cell was then set to open-circuit (④ in Fig. 3a). Particle E continued to shrink during this period of time (panel #vii). Finally, the cell was subjected to another short cycle of

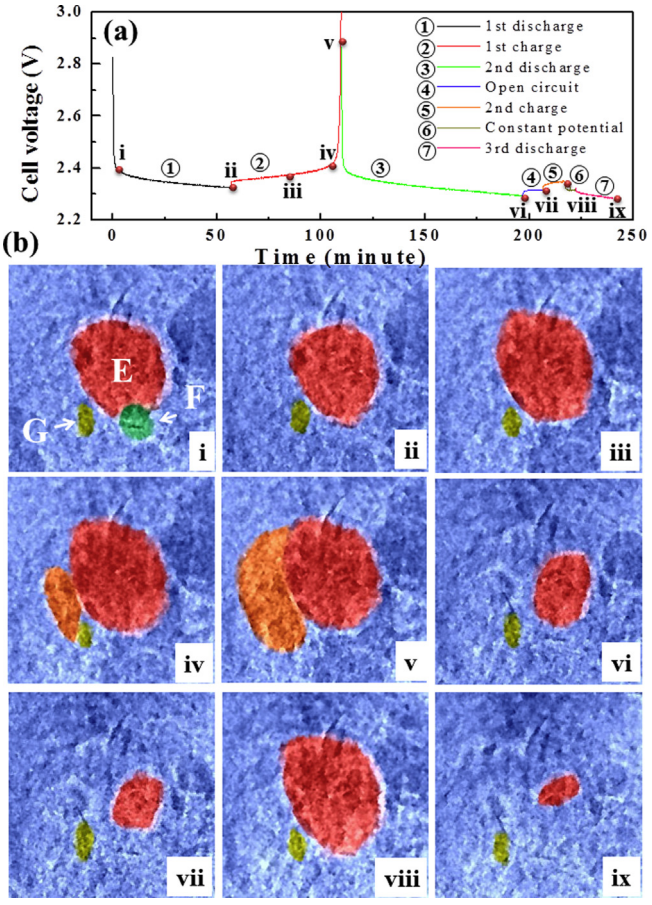

Fig. 3. TXM analysis of S electrode subjected to a series of electrochemical lithiation/de-lithiation cycles shown in (a); (b) snapshots of an area containing three S particles respectively indexed as E, F and G. The moments when the snapshots taken are marked in (a) with the same numbers.

lithiation/de-lithiation, where particle E exhibited size enlargement and reduction accordingly (panels #viii and #ix). It is interesting to note that the size of particle G remained invariant throughout the process. It is most likely an impurity particle.

Particle size growth resulting from re-deposition of PS may be described in a way analogous to the dissolution equation described above, giving a similar time-dependent equation for the deposition:

$$\frac{D}{D_0} - 1 = \left(\frac{2f'}{\rho D_0}\right)\cdot t = k'\cdot t \tag{4}$$

where f' is the deposition flux and k' is the normalized expansion rate constant (min^{-1}). In Fig. 4, we plots the size variations, expressed in $[D/D_0 - 1]$ according to Equation (4), of particle E versus time during two de-lithiation periods, including the first and second charge (de-lithiation) periods (② and ⑤ in Fig. 3a). As shown, in both cases, linear correlation between $[D/D_0 - 1]$ and time can be established. Furthermore, comparing the line slopes, it is noted that the second-charge period gives a greater slope, and hence a greater k' than the first-charge period. This difference may be attributed to the combination of a smaller initial particle size D_0 and a higher flux f'. The latter results form a higher PS concentration in the electrolyte during the later stage of cycling.

Panels #i through #iii in Fig. 3b show that the large E particle grows at the expense of small F particle. It depicts an interesting electrochemically driven "sintering" process resulting from dissolution/re-deposition cycles of PS species. During the cycling, we typically observed (such as from panel #ii to #iii or from #vii to #viii in Fig. 3b) that size-growth of existing particles takes place prior to the formation of new particles during de-lithiation. This sequence may suggest that nucleation to form new particles encounters a higher energy barrier and occurs at a slower rate so that re-deposition preferentially takes place on the existing particles. That is, the re-deposition process is said to be nucleation-limited. This may lead to two consequences that could have strong impact on the performance of the S electrode. Firstly, the large particles that have not completely been dissolved during the lithiation cycle would grow into a larger size upon subsequent de-lithiation cycle. As a result, there is expected continuous reduction in the total number of the particles and increase in average particle size after repeated cycles. Aggregation of electrode active mass will cause reduction in the overall electrolyte/solid contact surface area, which in turn leads to gradual deterioration in the rate performance of the battery.

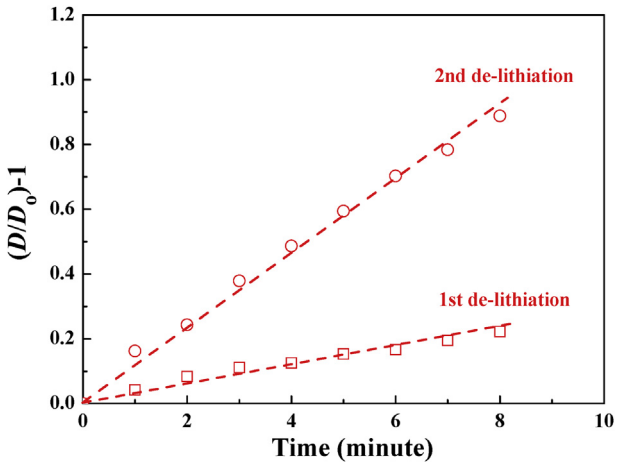

Fig. 4. Particle size data for a selected large particle (particle E in Fig. 3b) during different de-lithiation cycles.

Secondly, the existing particles may exhibit enormous cyclic dimensional variations. This is clearly demonstrated among panels #vii through #ix in Fig. 3b. As mentioned earlier, the theoretical molar volume increases by 80% between S_8 and Li_2S, which corresponds to one-dimensional expansion $(D/D_0 - 1)$ of 21%. In contrast, the particle E exhibits an increase in particle size by 116% between panel #vii and #viii, followed a reduction by 65% between panel #viii and #ix. These dimensional variations both far exceed the theoretical value. The large cyclic dimensional variations of the particles upon cycling may easily induce high stress to cause loosening of electrode structure, leading to deteriorating electric contact among different components and hence fast capacity fading.

In order to enhance the cycle life of S electrode, instead of using bare large S particles as in the present study, it has nowadays been a common practice to embed S inside the pores of porous carbon materials. The entrapment of S inside the pores has been meant to slow down diffusion of dissolved PS species out of the electrodes. Dissolution/re-deposition of PSs inside the pores will not cause volumetric variations due to physical constraint imposed by the C walls. However, dissolution/re-deposition of the PS species outside the pores may still impose threat to the cycle life of the electrode. It would be highly beneficial to introduce favorable nucleation sites, such as the particle G shown in Fig. 3b, into the electrode matrix for facilitating PS re-deposition so that S/PS particles deposited outside the pores may remain in high dispersion upon cycling. On the one hand, it can give large electrolyte/solid interfacial area and, on the other, it may help to avoid enormous dimensional variations associated with segregated large particles.

4. Conclusions

The dynamics of PS dissolution and re-deposition of S electrode in Li–S cell has been investigated by analyzing, with in-operando TXM, the morphological variations of S particles in working cells that were subjected to different depths of charge/discharge. The kinetic aspects of these processes are treated in a quantitative manner with classical theory. Extensive dimensional variations of S particles have been observed to result from PS dissolution/re-deposition. As reflected by the particle shrinking rate, the dissolution rate of PS exhibits complex dependence on Li stoichiometry. PS re-deposition is nucleation-limited, leading to considerable aggregation of the S-containing active mass and enormous dimensional variations of active particles. These two consequences may impose threat to the cycle stability of the electrode. Possible benefit of introducing favorable nucleation sites is discussed.

Acknowledgment

This work is financially supported by National Science Council Taiwan under contract number NSC 101-2221-E-002-160-MY3, National Taiwan University, National Synchrotron Radiation Research Center and Industrial Technology Research Institute.

Appendix A. Supplementary data

Supplementary data related to this article can be found at http://dx.doi.org/10.1016/j.jpowsour.2014.04.003.

References

[1] E. Peled, H. Yamin, Prog. Batteries Sol. Cells 5 (1984) 56–58.
[2] X. Ji, L.F. Nazar, J. Mater. Chem. 20 (2010) 9821–9826.

[3] P.G. Bruce, L.J. Hardwick, K.M. Abraham, MRS Bull. 36 (2011) 506–512.
[4] G. Zhou, D.W. Wang, F. Li, P.X. Hou, L. Yin, C. Liu, G.Q. Lu, I.R. Gentlc, H.M. Cheng, Energy Environ. Sci. 5 (2012) 8901–8906.
[5] T. Lin, Y. Tang, Y. Wang, H. Bi, Z. Liu, F. Huang, X. Xie, M. Jiang, Energy Environ. Sci. 6 (2013) 1283–1290.
[6] J.H. Shin, E.J. Cairns, J. Electrochem. Soc. 155 (2008) A368–A373.
[7] S.E. Cheon, K.S. Ko, J.H. Cho, S.W. Kim, E.Y. Chin, H.T. Kim, J. Electrochem. Soc. 150 (2003) A800–A805.
[8] H.S. Ryu, H.J. Ahn, K.W. Kim, J.H. Ahn, K.K. Cho, T.H. Nam, J.U. Kim, G.B. Cho, J. Power Sources 163 (2006) 201–206.
[9] H. Yamin, J. Penciner, A. Gorenshtein, M. Elam, E. Peled, J. Power Sources 14 (1985) 129–134.
[10] H. Yamin, A. Gorenshtein, J. Penciner, Y. Sternberg, E. Peled, J. Electrochem. Soc. 135 (1988) 1045–1048.
[11] J.K. Akridge, Y.V. Mikhaylik, N. White, Solid State Ionics 175 (2004) 243–245.
[12] F. Wu, J. Chen, R. Chen, S. Wu, L. Li, S. Chen, T. Zhao, J. Phys. Chem. C 115 (2011) 6057–6063.
[13] Y. Diao, K. Xie, S. Xiong, X. Hong, J. Electrochem. Soc. 159 (2012) A421–A425.
[14] C. Barchasz, F. Molton, C. Duboc, J.C. Leprêtre, S. Patoux, F. Alloin, Anal. Chem. 84 (2012) 3973–3980.
[15] S.S. Zhang, J. Power Sources 231 (2013) 153–162.
[16] N.A. Cañas, S. Wolf, N. Wagner, K.A. Friedrich, J. Power Sources 226 (2013) 313–319.
[17] M.U. Patel, R. Demir-Cakan, M. Morcrette, J.M. Tarascon, M. Gaberscek, R. Dominko, ChemSusChem 6 (2013) 1177–1181.
[18] S.C. Chao, Y.C. Yen, Y.F. Song, Y.M. Chen, H.C. Wu, N.L. Wu, Electrochem. Commun. 12 (2010) 234–237.
[19] S.C. Chao, Y.F. Song, C.C. Wang, H.S. Sheu, H.C. Wu, N.L. Wu, J. Phys. Chem. C 115 (2011) 22040–22047.
[20] J. Nelson, S. Misra, Y. Yang, A. Jackson, Y. Liu, H. Wang, H. Dai, J.C. Andrews, Y. Cui, M.F. Toney, J. Am. Chem. Soc. 134 (2012) 6337–6343.
[21] M. Winter, J.O. Besenhard, Electrochim. Acta 45 (1999) 31–50.